Shear-induced laning transition in a confined colloidal film

Sascha Gerloff, Tarlan A. Vezirov, and Sabine H. L. Klapp
Institut für Theoretische Physik, Hardenbergstrasse 36, Technische Universität Berlin, D-10623 Berlin, Germany
(Received 19 January 2017; revised manuscript received 10 May 2017; published 20 June 2017)

Using Brownian dynamics simulations, we investigate a dense system of charged colloids exposed to shear flow in a confined (slit-pore) geometry. The equilibrium system at zero flow consists of three well-pronounced layers with a squarelike crystalline in-plane structure. We demonstrate that, for sufficiently large shear rates, the middle layer separates into two sublayers where the particles organize into moving lanes with opposite velocities. The formation of this "microlaned" state results in a destruction of the applied shear profile; it also has a strong impact on the structure of the system, and on its rheology as measured by the elements of the stress tensor. At higher shear rates, we observe a disordered state and finally a recrystallization reminiscent of the behavior of bilayer films. We also discuss the system size dependence and the robustness of the microlaned state against variations of the slit-pore width. In fact, for a pore width allowing for four layers, we observe a similar shear-induced state in which the system splits into two domains with opposite velocities.

DOI: 10.1103/PhysRevE.95.062605

I. INTRODUCTION

Dense colloidal suspensions subject to strong spatial confinement can form solidlike structures not seen in their bulk counterparts. A well-established example are hard-sphere-like colloidal particles between two parallel plates with a distance L_z of the order of the particle diameter d [1–4]. Depending on the commensurability of L_z and d (as well as the chemical potential), one observes the formation of n layers with either square or hexagonal lattice symmetry within the plane parallel to the plates [with alternating order $n\square$, $n\triangle$, $(n+1)\square$, ...] [1,2]. Moreover, at high densities exotic structures such as buckled and rhombic crystals do occur [1]. While the equilibrium behavior of strongly confined suspensions is well understood for many colloidal and molecular systems, the interplay between particle packing and shear flow remains surprisingly elusive. This contrasts the fact that sheared films are of major relevance in many industrial processes involving surface coatings, lubricants, and microfluidic devices.

A number of recent experimental and numerical studies have focused specifically on *hydrodynamic* effects occurring due to the interplay of confinement and flow [5–11]. Hydrodynamic effects have also been considered in the context of slit-pores with modulated pore widths [12–15] and confined active particles [16–18]. However, these studies typically consider dilute systems and relatively wide gaps involving a bulklike region (at zero flow) in the middle region [8–10]. Another set of studies considers the flow of non-Brownian particles (no thermal fluctuations), including their frictional properties as a function of L_z [19,20].

In the present paper, we are interested in the shear-induced behavior of a thin film of Brownian spheres, which, already in equilibrium, forms a crystalline lateral structure with square symmetry. Specifically, we consider the case of $n = 3$ layers. The system is studied on the basis of overdamped Brownian dynamics (BD) simulation without hydrodynamic interactions (following various earlier studies on dense systems under flow [21–24]). The particles interact via screened Coulomb interactions (matched to a real, silica system [25,26]), and the confining walls are considered as smooth on the particle scale. Shear is then imposed via a force acting on each particle, which only depends on the distance relative to the walls.

The present investigation extends earlier numerical and theoretical studies by some of us in which we focused on shear-induced transitions in bilayer systems [27,28] and, in particular, their description within the Frenkel-Kontorova model for solid friction [29]. From the perspective of a shear-driven bilayer, the trilayer film can be seen as a first step toward the third dimension. Moreover, as we will demonstrate, the trilayer film displays a novel effect that was already briefly mentioned in Refs. [28,29], and which we think is typical for sheared *thin* films: This effect consists of the formation of a state in which the particles in the middle layer organize into *lanes* along the flow direction. Laning is a typical nonequilibrium effect that occurs quite generically in binary systems of particles driven in opposite directions (such as in dusty plasmas [30,31], granular matter [32], pedestrian and ant dynamics [33–35], as well as oppositely charged colloids driven by an electric field [36,37]). In the present case, the driving force is represented by the shear flow generating competing effects on the particles in the middle layer. Moreover, the laning is accompanied by a transformation of the (originally flat) middle layer into two sublayers. This is in sharp contrast to the behavior of bilayers (and also of bulk suspensions), where the layers always remain flat [21]. In our system, the laned state occurs at shear rates in between the initial square state and the subsequent shear melting. Interestingly, a similar effect (stripe formation and related "buckling") has been reported in the context of experiments [6] of strongly confined hard-sphere suspensions.

The paper is organized as follows. In Sec. II, we describe our model system as well as some details of the computer simulations. Numerical results are presented in Sec. III, where we start by describing the overall dynamical behavior, followed by a detailed discussion of the shear-induced laning transition, the resulting single-particle dynamics, and the implications for the shear stress. Additionally, we present results for a system with four layers, where we observe a similar laned state. Finally, we summarize and conclude in Sec. IV. In the three Appendixes, we provide further simulation results concerning the stability of the laned state against variation of the system size, confinement width, and initial conditions.

II. MODEL AND SIMULATION DETAILS

Following previous studies [27,28], we consider a model colloidal suspension where two spherical particles (diameter d) with distance r_{ij} interact via a combination of a repulsive Yukawa potential, $u_{\rm Yuk}(r_{ij}) = W \exp\left[-\kappa r_{ij}\right]/r_{ij}$, and a repulsive soft-sphere potential, $u_{\rm SS}(r_{ij}) = 4\epsilon(d/r_{ij})^{12}$.

The interaction parameters are set to $W/(k_{\rm B}Td) \approx 123$ (where $k_{\rm B}T$ is the thermal energy), and the inverse Debye screening length is set to $\kappa d \approx 3.2$ (for details, see Refs. [25,26]). Spatial confinement is modeled by two plane parallel, smooth, uncharged surfaces separated by a distance L_z along the z direction and of infinite extent in the xy plane. We employ a purely repulsive fluid-wall potential [27],

$$u^{(\pm)}_{\rm wall}(z_i) = \frac{4\pi\epsilon_w}{5}\left(\frac{d}{z_i \pm L_z/2}\right)^9, \tag{1}$$

where z_i is the z position of particle i. The dimensionless coupling parameter ϵ_w/k_BT is set to 1. This choice of potential is motivated by previous investigations of the equilibrium structure, where we found very good agreement with experiments [25,26]. Our investigations are based on standard BD simulations in three dimensions, where the position of particle i is advanced according to [38]

$$\mathbf{r}_i(t+\delta t) = \mathbf{r}_i(t) + \frac{D_0}{k_BT}\mathbf{F}_i(t)\delta t + \delta\mathbf{W}_i + \dot\gamma z_i(t)\delta t\mathbf{e}_x. \tag{2}$$

Here, $\mathbf{F}_i$ is the total conservative force acting on particle i, and $\delta\mathbf{W}_i$ denotes a random Gaussian displacement with zero mean and variance of $2D_0\delta t$ for each Cartesian component. The friction constant is $(D_0/k_BT)^{-1}$, where D_0 is the short-time diffusion coefficient. The time scale of the system is set to $\tau = d^2/D_0$, which defines the so-called Brownian time. We impose a linear shear profile [see the last term in Eq. (2)] representing flow in the x direction and gradient in the z direction, characterized by a uniform shear rate $\dot\gamma$ [24,39]. This ansatz seems plausible for systems in which the impact of the walls on the driving mechanism can be neglected, such as charged colloids confined between likewise charged, smooth walls [40,41]. For this situation, the distance between the colloids and the wall is naturally rather large, suggesting that the motion of the colloids is not directly coupled to that of the particles comprising the wall. Thus, one may assume that the shear flow away from the wall is approximately linear. We note, however, that despite the application of a linear shear profile, the real, steady-state flow profile can be nonlinear [42]. Furthermore, to reduce the computation time, we neglect hydrodynamic interactions. We focus on a strongly confined ($L_z = 3.2d$) and dense ($\rho d^3 = 0.85$) system with 1587 particles. The resulting lateral width of the simulation cell then follows as $L \approx 24.2d$. Periodic boundary conditions were applied in the flow (x) and vorticity (y) directions. The time step is set to $\delta t = 10^{-5}\tau$. After an equilibration period of 10^7 steps (i.e. 100τ), the system relaxes (in agreement with our expectations [26,28]) in a trilayer with square in-plane order. Then the shear force is switched on. After starting the shearing, the simulation was carried on for an additional period of 100τ. During this time, the steady state is reached. Only after these preparations did we start to analyze the considered systems.

III. NUMERICAL RESULTS

In this section, we present our numerical results for the dynamical behavior of the shear-driven trilayer. We start by reviewing the overall behavior, followed by a detailed discussion of the novel, *microlaned* state of the middle layer, the associated single-particle dynamics, and the resulting rheological behavior. Finally, we briefly discuss a system consisting of four layers, displaying a similar laned state.

A. Overview

As a first overview of the shear-induced structural changes, we present in Fig. 1 BD simulation snapshots at representative values of the dimensionless shear rate $\dot\gamma\tau$. We can identify four different states. The first one is a laterally crystalline state with *square* in-plane ordering in each of the three layers. This state corresponds to the equilibrium configuration ($\dot\gamma = 0$) at the thermodynamic conditions considered, and it persists at small shear rates such as $\dot\gamma\tau = 10$ [see Fig. 1(a)]. The degree of (local) quadratic translational order in each layer is quantified by the order parameter Ψ_n with $n = 4$, with Ψ_n being generally defined as

$$\Psi_n = \left\langle \frac{1}{N_L}\sum_{i=1}^{N_L}\frac{1}{N_i^b}\left|\sum_{j=1}^{N_i^b}\exp(in\theta_j)\right|\right\rangle. \tag{3}$$

In Eq. (3), N_L describes the instantaneous number of particles, and N_i^b is the number of neighbors of particle i in the considered layer (the position of each layer can be extracted from the density profile; see below). The value of N_i^b was calculated from the intralayer pair correlation function by determining the radius related to the first minimum of the

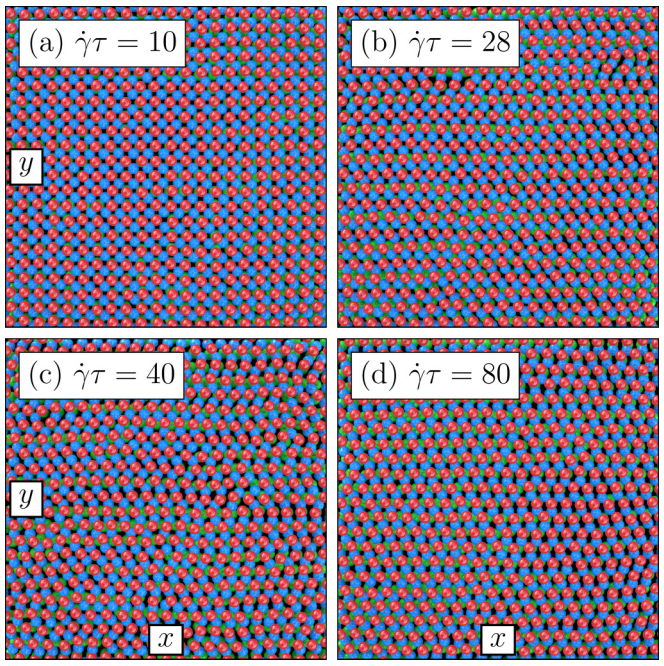

FIG. 1. (a)–(d) Simulation snapshots of the xy plane at ρd^3=0.85 and $L_z = 3.2d$ for different shear rates. The red (blue, green) circles represent particles of the upper (middle, lower) layer.

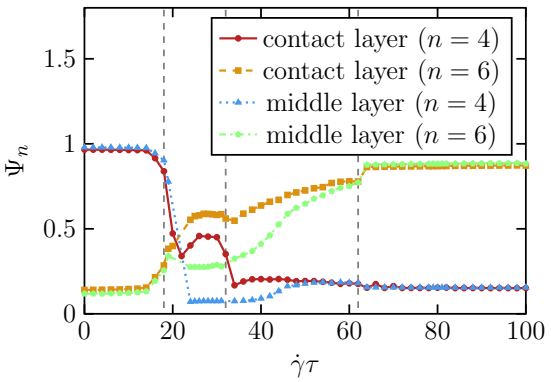

FIG. 2. In-plane order parameter for square (Ψ_4) and hexagonal (Ψ_6) symmetry as a function of the dimensionless shear rate $\dot{\gamma}\tau$. The order parameter was calculated separately for the middle and the contact layers.

intralayer pair correlation function [27]. Perfect square or hexagonal order is characterized by $\Psi_{4/6} = 1$, respectively.

Results for Ψ_4 and the hexagonal order parameter Ψ_6 for the individual layers as functions of the shear rate are plotted in Fig. 2. For completeness, we also present in Fig. 3 the density profile in the z direction, $\rho(z) = \langle N(z)/N\Delta z\rangle$ [where $N(z)$ is the instantaneous number of particles at a given distance z, and Δz defines the bin width]. In the initial state, all layers are characterized by a high degree of squarelike order (and, correspondingly, very small values of Ψ_6). This changes at $\dot{\gamma}\tau \approx 18$, where we observe a sudden decrease of Ψ_4. A visualization of the system's structure in the subsequent state is given in Fig. 1(b), suggesting, at first glance, a substantial loss of in-plane order as compared to the initial state. However, as we will discuss in more detail in Sec. III B, this state is characterized by a "splitting" of the middle layer into two sublayers, where the particles in the two sublayers organize into lanes. Therefore, the top view provided in Fig. 1(b) provides only partial information. The splitting can already be seen from the density profile (see Fig. 3), which displays, at $\dot{\gamma}\tau = 28$, a double peak in the middle of the slit. This contrasts the single middle peak observed at other shear rates. The third state [see Fig. 1(c)] has an overall disordered appearance,

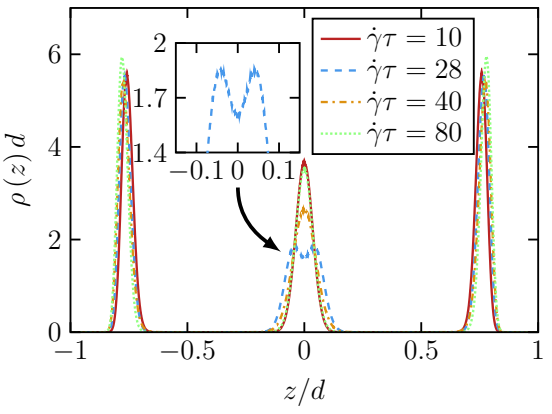

FIG. 3. Density profiles along the shear gradient (and confinement) direction for different shear rates. In the inset, the middle peak of the density profile for $\dot{\gamma}\tau = 28$ is magnified, revealing the double-peak structure.

with the degree of hexagonal order being somewhat larger than the values of Ψ_4. The corresponding density distribution (see Fig. 3) is characterized by an unsplit yet rather broad peak at the middle position. This "molten" state resembles the one seen in shear-driven *bilayer* systems at shear rates directly beyond the quadratic regime [27]. This correspondence also holds for even higher shear rates where the trilayer system (in analogy to the bilayer) recrystallizes into a state with hexagonal in-plane order in all layers [see Figs. 1(d) and 2].

We can thus conclude that while the limiting behavior of the trilayer at low and high shear rates, respectively, is identical to that in bilayer systems [27], the breakdown of ordering at intermediate shear rates shows pronounced differences. In the next subsection, we analyze in more detail the structure in this "microlaned" state.

B. Laning transition

To better understand the nature of the laned state, we present in Fig. 4 snapshots only of the middle layer at the same shear rates considered already in Fig. 1. We note that, independent of the precise value of $\dot{\gamma}\tau$, the middle layer has a certain width involving particles located at z values slightly above or below the middle plane at $z = 0$. In Fig. 4 we distinguish between these particle using different colors. The snapshots at low and high shear rates reveal, as expected, the occurrence of quadratic [Fig. 4(a)] and hexagonal [Fig. 4(d)] order, respectively, with the colors of the particles suggesting an essentially random distribution of positive and negative z values within the middle plane. This mixed distribution also holds in the shear-molten state [Fig. 4(c)]. In contrast, Fig. 4(b) clearly demonstrates a "micro" phase separation of the particles: The two different types arrange into narrow "lanes" along the flow (x) direction, with the quadratic order between particles of

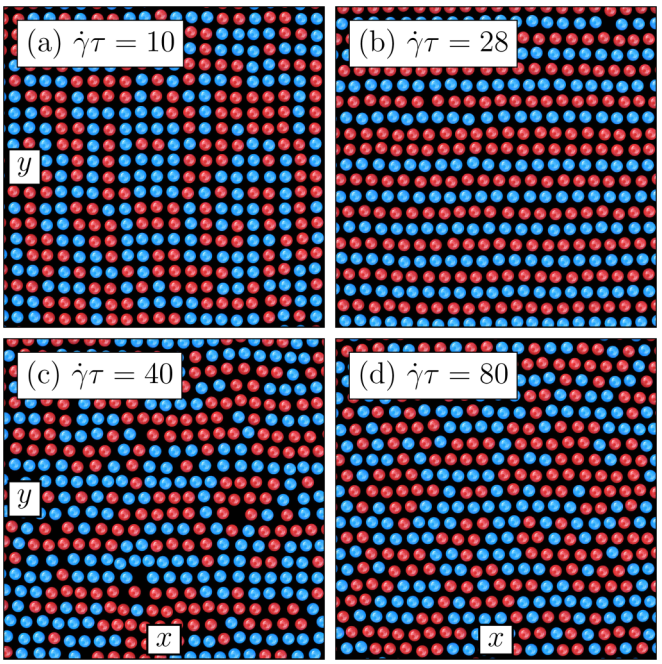

FIG. 4. (a)–(d) BD simulation snapshots of the middle layer at $\rho d^3 = 0.85$ and $L_z = 3.2d$ for different shear rates. The blue (red) circles represent particles with $z > 0$ ($z < 0$).

different lanes being much less pronounced than in the initial quasiequilibrium state. This separation explains the splitting of the density peak observed at $\dot{\gamma}\tau = 28$ (see Fig. 3), as well as the accompanying decrease of the order parameter Ψ_4 (Fig. 2).

From a physical point of view, the occurrence of the lanes may not be surprising: We recall that, in the present shear geometry, particles at equal distance from the middle plane experience an *oppositely* directed shear force via the externally controlled flow profile. The occurrence of a "laning transition" in binary systems of oppositely driven particles is indeed a well-established phenomenon that has been observed in a wide variety of systems, including colloids and pedestrians [34,43].

Inspired by the numerous studies of laning in colloidal systems, we define here a laning order parameter (see, e.g., [43]) addressing the particles in the middle layer. We first assign to each particle the parameter ϕ_i, which is chosen to be 1 if the lateral distance $|y_i - y_j|$ to all particles of the adjacent *sublayer* j is larger than the average distance $r_{\text{lane}} = \rho^{-1/3}/2$. Otherwise, ϕ_i is set to 0. The laning order parameter is then defined as

$$\Phi = \left\langle \frac{1}{N_L^{\text{mid}}} \sum_{i=1}^{N_L^{\text{mid}}} \phi_i \right\rangle. \tag{4}$$

In Eq. (4), N_L^{mid} denotes the number of particles within the middle layer.

Numerical results for Φ as a function of the shear rate are plotted in Fig. 5. One clearly recognizes a regime of shear rates ($18 \lesssim \dot{\gamma}\tau \lesssim 32$) with a strong degree of laning, consistent with the observation in Fig. 4(b). We note that the results for Φ depend somewhat on the system size. This aspect is discussed in more detail in Appendix A. We find that the range of shear rates of the laned state decreases slightly upon an increase of the system size N. However, the general effect remains even for much larger systems ($N = 6627$). We have also tested the robustness of the laned state against small variations of the slit-pore width L_z (see Appendix B). The test simulations reveal that, upon decreasing L_z from its current value ($L_z = 3.2d$), the laned state vanishes because the lateral pressure in the x and y directions decreases. For larger L_z, the quadratic equilibrium configuration is no longer stable,

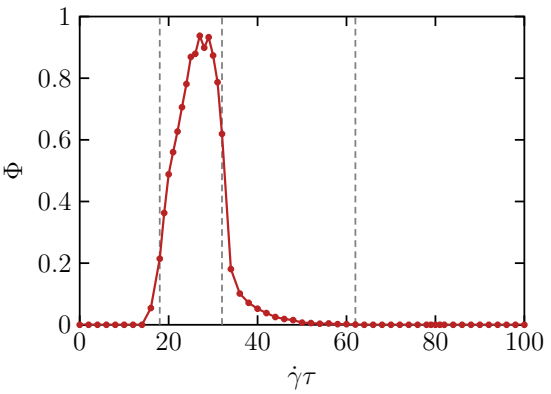

FIG. 5. Laning order parameter within the middle layer as a function of the shear rate.

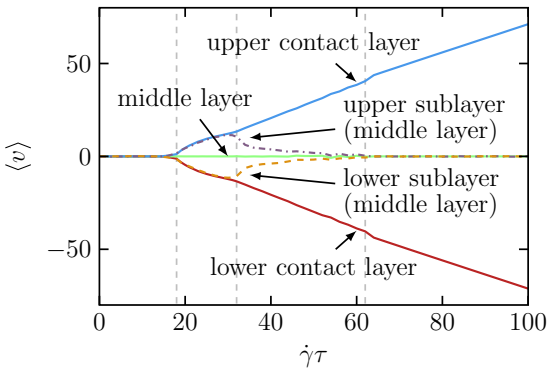

FIG. 6. Velocity of the center of mass of all three layers as well as the sublayers of the middle layer.

and a hexagonal in-plane order is favored, limiting the range of suitable L_z.

The separation of the system into lanes also explains the relatively low values of the translational order parameters in this state: The results in Fig. 2 have been obtained by averaging over the entire layers, which, for the middle layer, clearly yields distorted results.

C. Single-particle dynamics

We now turn to dynamical aspects associated with the shear-induced structural behavior discussed so far. To start with, we consider in Fig. 6 the velocity of the center of mass of each layer (and sublayer, where appropriate).

The initial, square state is characterized by zero motion of all three layers; in other words, the particles are "locked" in the regular potential valleys formed by the neighboring layers. Upon increasing the shear rate toward the laned, molten, and hexagonal states, the two outer layers start to move, while the *average* velocity in the middle layer remains zero. This is expected in view of our shear geometry, which implies that the shear force vanishes at $z = 0$. Contrary to this average motion, however, the sublayers formed in the laned state do move, as Fig. 6 reveals. In particular, the corresponding velocities are close to those of the outer layers. Thus, the velocity profile within the middle layer transforms into two "domains" with opposite velocities. In the molten state, we still observe sublayer motion, but the corresponding velocities "decouple" from those of the outer layers (reflecting a gradual disappearance of lanes). As a consequence, the sublayer velocities decrease to zero upon approaching the hexagonal state. We thus see that the laned and molten states, which were hardly distinguishable from their configurations (see Fig. 1), differ clearly in their velocity profiles.

Further information on the dynamics on the particle level is provided by investigating typical trajectories. Specifically, we consider in Fig. 7 the position of typical particles in the flow (x) direction. The colors indicate the corresponding z position. The thick horizontal line in part (a), which is composed of aligned trajectories of multiple particles, reflects the "locking" of the particles in their lattice position at low shear rates. In the other extreme case [the hexagonal state, part (d)], we observe uniform flow behavior of the particles in the outer layers, as well as the rest of the ones in the middle plane.

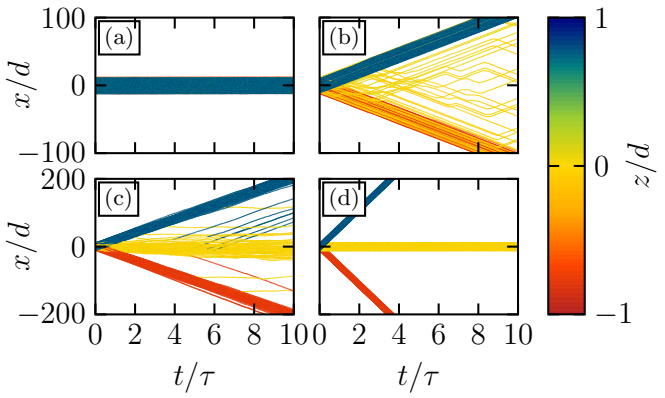

FIG. 7. Trajectories of arbitrarily chosen particles at different shear rates corresponding to the four states. The colors indicate the position in the z direction (see the color bar on the right).

Regarding the intermediate states, the trajectories reflect some degree of nonuniform behavior. In particular, we observe in the lane states trajectories with oscillations around $x = 0$ at early times; these oscillations correspond to particles hopping between the sublayers of the middle plane (and thus hopping back and forth). In the molten state, the behavior becomes more uniform; in particular, a large number of particles in the middle plane rests. This indicates that the system approaches a uniform velocity profile similar to the hexagonal state.

A further characteristic dynamical feature of each state is the mean-squared displacement (MSD) relative to the center of mass. Here we focus on the MSD in the middle layer, since this layer shows the greatest variety in order and dynamics. Taking into account that the center-of-mass velocity in this layer is zero, and specializing on the flow (x) direction, we define the MSD according to

$$\mathrm{MSD}_x = \left\langle \frac{1}{N_L^{\mathrm{mid}}} \sum_{i=1}^{N_L^{\mathrm{mid}}} [x_i(t) - x_i(0)]^2 \right\rangle, \tag{5}$$

where N_L^{mid} is the number of particles in the middle layer. Results for the MSD in the four different states are plotted in Fig. 8. In the square ($\dot\gamma\tau = 10$) and hexagonal ($\dot\gamma\tau = 80$) state, respectively, the MSD increases somewhat with time, particularly for $t > 10\tau$. However, it remains smaller than $1d$ throughout the simulation time considered ($t < 200\tau$). This reflects the persistent trapping of the particles at the sites of the square or hexagonal lattice. We thus expect that the diffusive behavior in the range $10\tau < t < 200\tau$ is transient.

In the shear-molten state, the long-time behavior of the MSD become diffusive (i.e., linear in time) at long times, as expected in a liquidlike state in the absence of any center-of-mass motion. The intermediate dynamics can be further analyzed in terms of an effective single-particle model describing a particle in a harmonic potential (mimicking the spatial confinement in the z direction) [27]. Here we rather focus on specific features of the laned state. The corresponding MSD behaves indeed differently. In particular, we observe a ballistic regime $\propto t^2$ at intermediate times. Such a ballistic time dependence also occurs for a free particle under shear flow [44], reflecting the presence of net (center-of-mass) motion. In the present case, the motion is performed by the two sublayers in which the middle layers split (see the nonzero velocities of the sublayers in Fig. 6). Having this in mind, it seems somewhat surprising that the MSD at later times becomes diffusive again. Recall, however, that the MSD defined in Eq. (5) involves *all* particles in the middle layer. This includes, in particular, particles jumping between the sublayers. An example is seen in Fig. 7(b), where the trajectories show particles of the middle layer switching their direction of motion. On the level of the MSD, these jumps (i.e., spontaneous changes of the direction of motion) manifest themselves as an *oscillatory*, yet *irregular*, time dependence, as may be verified from Fig. 9, where we plot the MSD of a single system (without averaging). Averaging over many systems then finally leads to the observed diffusive behavior.

D. Rheological properties

To complete the picture of the three-layer system, we have also investigated rheological properties as probed by the components σ_{mn} (with $n,m \in x,y,z$) of the stress tensor $\boldsymbol{\sigma}$. The components were calculated (consistent with [28]) via the

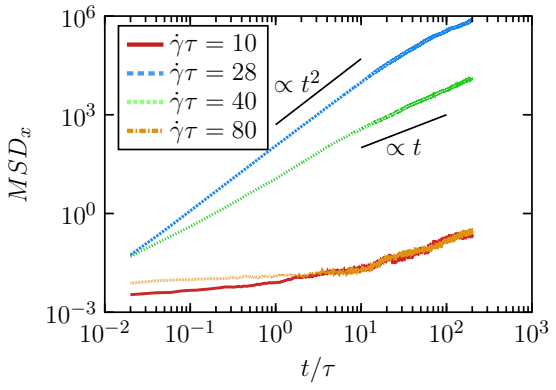

FIG. 8. Mean-squared displacement in the flow direction relative to the center of mass of the particles in the middle layer at different shear rates (in units of d^2).

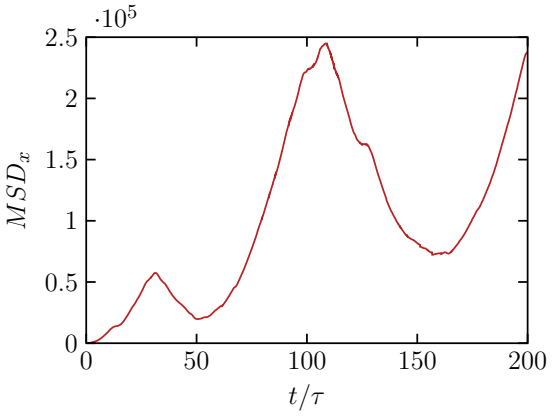

FIG. 9. MSD_x of one single system at $\dot\gamma\tau = 28$ (in units of d^2). For the calculation, only the particles from the middle layer were considered.

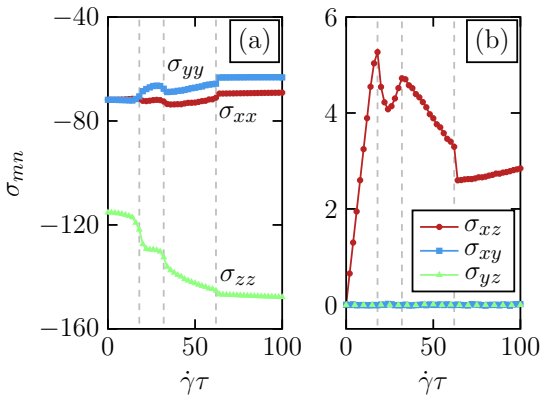

FIG. 10. Components of the stress tensor as a function of the applied shear rate.

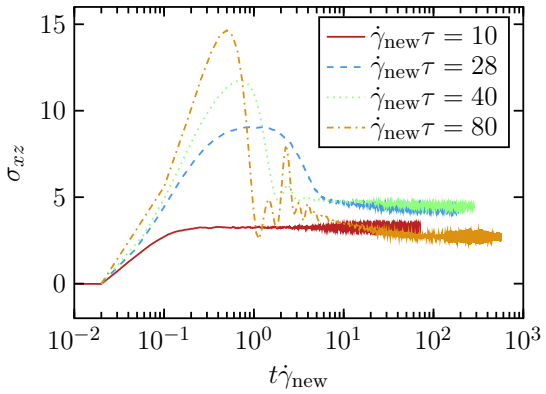

FIG. 11. Stress-strain relations in the colloidal trilayer for different shear rates $\dot{\gamma}_{\rm new}$, starting from the equilibrium (square) configuration. The shear is switched on at $t/\tau = 0.01$.

virial expression

$$\sigma_{mn} = \left\langle \frac{1}{V} \sum_i \left[\sum_{j>i} F_{m,ij} n_{ij} + \delta_{nz}\delta_{mz}\, \sigma_w(z_i) \right] \right\rangle, \quad (6)$$

where δ_{nm} is the Kronecker delta, $F_{m,ij}$ is the m component of the two-particle interaction forces, n_{ij} is the n component of $\mathbf{r}_{ij}$, and σ_w is the stress contribution from the confining walls. The latter is defined as

$$\sigma_w(z_i) = -\frac{\partial u^{(\pm)}_{\rm wall}(z_i)}{\partial z_i}(z_i \pm L_z/2). \quad (7)$$

The kinetic contributions were neglected. In fact, in the framework of *overdamped* BD simulations, the only nonvanishing contributions to the kinetic stress are given by the ideal gas contribution, which are $\sigma^{\rm ideal}_{nn} = -P = -Nk_BT/V$ for all diagonal components and zero for all others. Results for the steady-state stress tensor [i.e., $\lim_{t\to\infty}\sigma_{mn}(t)$] as functions of the dimensionless shear rate are presented in Fig. 10. We consider first the diagonal components (a), the negative values of which correspond to the pressure tensor components of the confined system. The equilibrium limit ($\dot{\gamma} \to 0$) is characterized by $\sigma_{xx} = \sigma_{yy}$, as expected in the fully symmetric quadratic state forming our starting configuration. The corresponding normal stress σ_{zz} is much larger in magnitude, a generic effect in strongly confined fluids. Upon increasing the shear rate, we find that all diagonal components σ_{mm} reflect, to some degree, the shear-induced transitions. As a general trend, the normal stress further increases in magnitude. We understand this as a consequence of the fact that, with increasing $\dot{\gamma}$, the distance between the layers increases progressively (see the density profiles in Fig. 3). This enables the particles to follow the flow more efficiently. At the same time, however, it brings more and more particles into the contact zone close to the walls, which, consequently, increases the overall repulsion. A further feature upon increasing $\dot{\gamma}$ is that, beyond the threshold toward the laned state, σ_{xx} and σ_{yy} deviate from one another, indicating a structural asymmetry between flow and vorticity direction.

We now turn to the nondiagonal components [see Fig. 10(b)]. The shear stress σ_{xz} reveals a strongly nonmonotonic behavior with several multivalued regimes where the shear rate corresponding to a certain stress value is not uniquely defined (as already reported earlier by us [28]). In particular, the ranges of $\dot{\gamma}$ where the stress decreases imply that the corresponding (laned or shear-molten) state is mechanically unstable and would not be observable in a simulation (or experiment) at constant stress. The other off-diagonal components (σ_{xy},σ_{yz}) remain zero for all shear rates.

Finally, we consider the relaxation of the (shear) stress after a sudden switch-on of a finite shear rate $\dot{\gamma}_{\rm new}$, starting from the equilibrium (square) configuration at $\dot{\gamma} = 0$. Toward that end, we plot in Fig. 11 the quantity σ_{xz} as a function of the strain $\dot{\gamma}t$ (with fixed $\dot{\gamma} = \dot{\gamma}_{\rm new}$). Similar to earlier investigations performed for a bilayer system [28], the shape of the stress-strain relation depends strongly on the state into which the quench is performed. In particular, for all shear rates beyond the quadratic regime, we observe a pronounced stress "overshoot," i.e., a maximum in the stress-strain relation. The strain corresponding to this maximum depends on $\dot{\gamma}_{\rm new}$; at the highest value considered, it is about 10%. This value can be related to the typical size of the nearest-neighbor cages in the quadratic state, which are broken by the shear [45]. We also note that the closer $\dot{\gamma}_{\rm new}$ is to the "critical" value ($\dot{\gamma}_c\tau \approx 18$) separating the quadratic and laned states, the longer is the time in which the stress relaxes toward its final, steady-state value.

Due to the finite relaxation time toward the final steady states, which can become rather large particularly close to the transitions, we expect the system to display hysteretic behavior. In Appendix C, we discuss the hysteresis of the shear stress for a successive increase and decrease of the shear rate starting from the quadratic and hexagonal steady state, respectively. We find that due to the finite relaxation time, the transitions between the steady states are shifted against each other in the two setups.

This is most notable for the transition from the melted to the hexagonal or laned state, respectively. Nevertheless, the system in both setups eventually reaches all steady states, suggesting that the appearance of the laned state, in particular, is independent of the initial configuration.

E. Toward multiple layers

To test whether the phenomenon of laning is restricted to three-layer systems, we have performed some simulations with

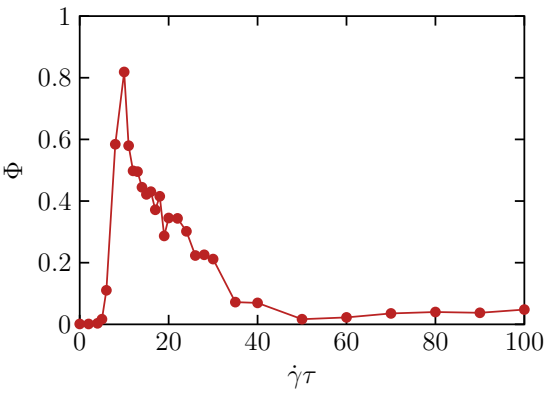

FIG. 12. Laning order parameter for the inner layers of a four-layer system ($L_z = 4.1d$).

four- and five-layer systems. The precise value of the slit-pore width is always chosen such that the equilibrium configuration is the quadratic state. Applying then the shear, we monitor the laning order parameter Φ [see Eq. (4)] of the inner layers. Toward that end, particles with the z position larger than the mean z position of the corresponding layer in equilibrium form the top sublayer, whereas all other particles form the bottom sublayer. We find that for the particular choice of $L_z = 4.1d$, the two inner layers indeed split up, leading to a laned state for a narrow range of shear rates. This is reflected by the sharp peak of Φ at $\dot{\gamma}\tau = 10$, seen in Fig. 12. We note that the "flank" on the right-hand side of the peak is a result of the finite number of particles in the system (see Appendix A for a systematic discussion of system size effects). Thus, the range of shear rates where laning occurs is smaller than that in the trilayer system. The small nonvanishing values of the laning order parameter for large shear rates should be considered as an artifact resulting from our definition of the sublayers. Inspecting the resulting steady-state configurations in real space, see Fig. 13, we find that the particles arrange in pyramid-like arrangements in the y-z direction, which move with similar velocity in the x direction. Similar to the laned state of the trilayer system, the bottom and top pyramids move in opposite directions.

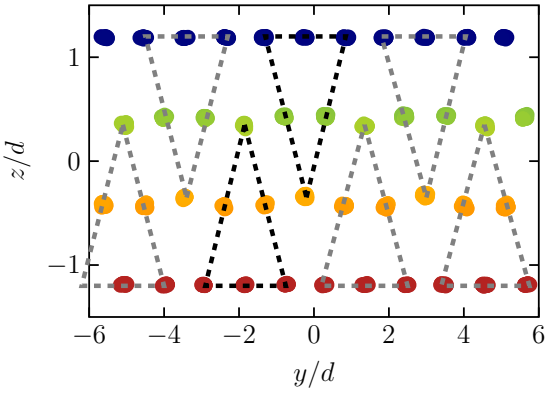

FIG. 13. Front view of the mean position of the particles for a system consisting of four layers ($L_z = 4.1d$, $\dot{\gamma}\tau = 10$). Similar to the laned state, the inner layers split up such that the particles organize in triangular configurations marked by the dashed lines.

Upon varying L_z around the value $L_z = 4.1d$, we still find laning (see Appendix B for a corresponding discussion of the three-layer system), but the corresponding ranges of $\dot{\gamma}$ are smaller than in the former case. For even wider widths allowing for five layers, we do not find a laned state at all at the considered density $\rho d^3 = 0.85$. Instead, the five quadratic layers formed at $\dot{\gamma}\tau = 0$ break up under shear, leading to four moving layers. Nevertheless, a laned state in a five-layer system may still occur for higher densities, where the lateral pressure (which generally stabilizes "buckled" configurations) is larger. However, a detailed study of the density dependence is beyond the scope of the current paper.

IV. CONCLUSIONS

Using BD simulations we have studied the structural and dynamical behavior of a thin colloidal film confined to a narrow slit-pore under planar shear flow (constant shear rate). We focused on a dense, strongly confined system whose equilibrium configuration consists of three well-pronounced layers with a squarelike crystalline in-plane structure. Compared to the previously studied case of two layers [27], the three-layer systems displays a novel dynamical state at shear rates beyond the depinning transition (i.e., the breakdown of the equilibrium structure). In this "microlaned" state, the middle layer splits into two sublayers with the particles being organized into lanes with opposite velocities. Closer inspection shows that the sublayers are "dragged" by the closest (bottom or top) outer layer, which essentially follows the externally applied flow profile. Overall, the situation corresponds to a plug flow with two domains, whose interface is within the middle layer. Upon further increase of the shear rate, the system enters a molten state and finally recrystallizes into an ordered state with hexagonal in-plane structure reminiscent of the behavior of the bilayer films [27].

By monitoring the components of the stress tensor, we find that the microlaned state is characterized by a negative slope of the shear stress as a function of the shear rate. This suggests that the microlaned state is, in fact, mechanically unstable and will not be observable in simulations (or experiments) at constant stress.

A similar phenomenon has been reported within an experimental study of strongly confined hard-sphere suspensions [6]. Specifically, the authors of Ref. [6] observe a shear-induced transition from an (initial) configuration consisting of four flat layers to a configuration consisting of three buckled layers, which are characterized by distinct velocities (the layers were distinguished by monitoring their velocity instead of their density profile). This latter configuration is explained by a "mismatch" of the osmotic pressure of the bath and the pressure (tensor) in the confined system corresponding to flat layers, which need to be balanced.

In light of these experimental findings, the occurrence of the microlaned state reported here may be interpreted as a transition from three flat layers to two buckled layers with different mean velocities (see Fig. 6). From that point of view, our results are qualitatively consistent with the observations of the aforementioned experiments. A detailed comparison is difficult since the experiments are carried out with the confined system being connected to a bulk suspension at

constant osmotic pressure, as well as at oscillatory shear. Still, the qualitative agreement may be taken as an indication that the shear-induced laned state is a characteristic feature of *thin* films of a few layers.

In fact, considering a system consisting of four layers, we find a very similar state where the system splits into two domains with opposite velocity. The range of suitable shear rates and slit-pore widths is smaller than in the trilayer case. However, we did not observe laning for a system consisting of five layers at the considered density. Whether or not this system displays laned (or "buckled") states at higher densities remains to be explored.

For future simulation studies, one important direction is to further investigate the robustness of the microlaned state for a larger parameter space. This concerns in particular the slit-pore width and the overall density. Already in equilibrium, variation of these parameters yields a complex phase diagram [1] with different crystalline structures. The impact of shear on these structures as a function of pore width and density has yet to be fully explored.

In this context, another intriguing question concerns the spatial dependence of the local shear rate and shear stress in the direction of the confinement. Toward that end, we note that, as reported in Refs. [5,46], the present method to calculate the stress [see Eq. (6)] is not suitable to resolve the spatial dependence, rather it leads to an inhomogeneous stress tensor. Instead one should use an appropriate alternative method of calculation, such as the method of planes (MOP) [47], or one should consider a system with hydrodynamic equations from the outset [46,48].

Another key question concerns the impact of hydrodynamic interactions on the "microlaned" state. The formation of lanes could be significantly enhanced or disturbed by the explicit introduction of solvent dynamics (which was neglected here), due to the small distances between the lanes and rather large velocities. However, in view of the similarity of the microlaned state to the buckled state observed in experiments [6], we expect hydrodynamic interactions to affect the time scales, but not the overall behavior of the system.

ACKNOWLEDGMENT

This work was supported by the Deutsche Forschungsgemeinschaft through SFB 910 (project B2).

APPENDIX A: SYSTEM SIZE DEPENDENCE OF THE LANED STATE

The laned state is characterized by a stripelike ordering of the middle layer in the flow direction, which may depend on the system size. To investigate if the laned state is indeed a finite-size effect, we have calculated the laning order parameter for additional systems with $N = 675, 1200$, and 6627 particles. Results are displayed in Fig. 14.

We find that laning in the middle layer can be observed for all considered system sizes. For very small systems ($N = 675$), one observes large values of the laning order parameter for a wide range of shear rates. Increasing the number of particles, the laned state shifts to smaller shear rates and the range of shear rates is slightly decreased. Nevertheless, the results show

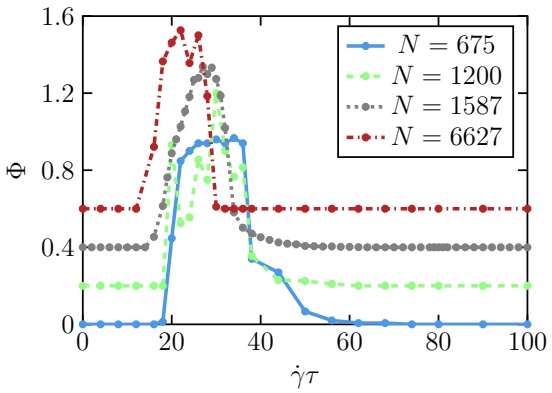

FIG. 14. Laning order parameter for systems with varying size $N = 675$, 1200, 1587, and 6627. For $N = 675$, 1200, and 6627, the laning order parameter was calculated for a single system, whereas for $N = 1587$ an ensemble average was taken (see Fig. 5). The graphs are shifted by 0.2 for clarity.

that the laned state is not a result of a finite size of the simulation box, but a physical phenomenon that persists for much larger systems.

APPENDIX B: CONFINEMENT WIDTH DEPENDENCE OF THE LANED STATE

In this Appendix, we explore the robustness of the laning transition against small variations of the pore width around the value $L_z = 3.2d$ chosen in the main part of the investigation. These calculations are carried out at constant overall density $\rho d^3 = 0.85$. The more physical strategy would be to vary L_z at constant lateral pressure $P_\parallel$ or constant normal pressure $P_\perp$. However, this technically means to change the ensemble from canonical to isobaric, which is beyond the scope of this study. In the present setup (constant $\rho d^3 = 0.85$), a slight increase of L_z implies an increase of the accessible volume in the z direction and a corresponding decrease in lateral directions. Thus the lateral pressure *within* the layers $P_\parallel$ increases with the confinement width, as shown in Fig. 15(b). In this figure, we have calculated this lateral pressure in equilibrium via

$$P_\parallel = \sum_{L=1}^{3} \left\langle -\frac{1}{V} \sum_{i=1}^{N_L} \sum_{j>i} F_{x,ij} x_{ij} \right\rangle, \tag{B1}$$

with N_L being the number of particles inside layer L. We note that in equilibrium, the pressure in the x and y directions is the same, as seen in Fig. 10(a).

In Fig. 15(a), we have plotted the laning order parameter for various widths of the confinement, $L_z/d = 3$, 3.05, 3.1, 3.15, 3.2, and 3.25. We find that the order parameter is largest at the upper limit of this range, consistent with our expectation that an increase of L_z in the considered range enhances the "buckling" or laning, respectively, and becomes weaker upon decreasing the width. For very small widths, $L_z \leqslant 3.05d$, the middle layer becomes strongly disordered, leaving only two pronounced outer layers.

Decreasing the confinement width also shifts the laned state toward larger shear rates, which can be explained by the fact that the stability of the quadratic state at $\dot{\gamma}\tau = 0$ increases

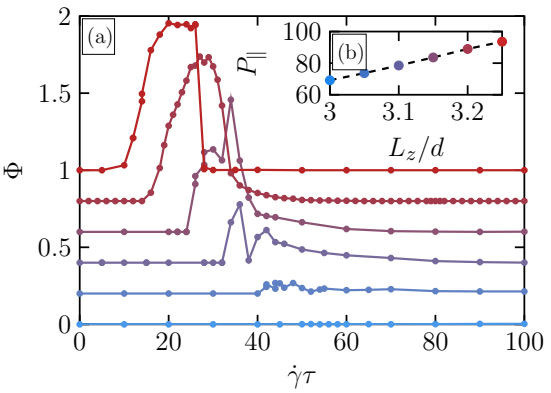

FIG. 15. (a) Laning order parameter for systems with varying confinement width $L_z/d = 3$, 3.05, 3.1, 3.15, 3.2, and 3.25 (bottom to top). For $L_z/d = 3$, 3.05, 3.1, 3.15, and 3.25, the laning order parameter was calculated for a single system, whereas for $L_z/d = 3.2$ an ensemble average was taken (see Fig. 5). The graphs are shifted by 0.2 for clarity. (b) The inset shows the lateral pressure within the layers $P_\parallel$ [see Eq. (B1)] in equilibrium ($\dot\gamma = 0$) depending on the confinement width L_z.

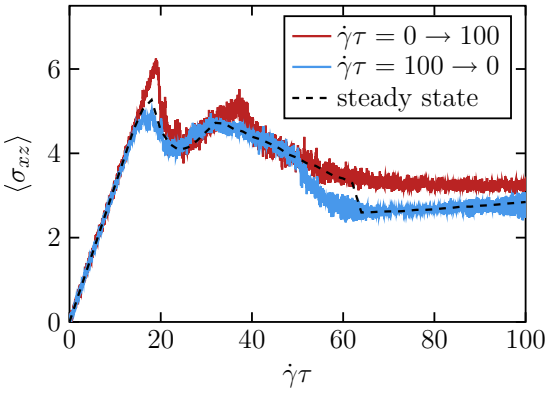

FIG. 16. Shear stress run averaged over ten systems starting from $\dot\gamma_{\text{initial}}\tau = 0, 100$ successively increasing or decreasing to $\dot\gamma_{\text{final}}\tau = 100, 0$ (red, blue) by small steps of $\Delta\dot\gamma\tau = 0.01$. The steady-state shear stress (black dashed) is plotted as a reference [see Fig. 10(b)].

(due to the strong compression of the layer) [29]. Overall, we find that the range of suitable confinement widths is limited by two different mechanisms. For small widths, $L_z < 3.1d$, the laned state vanishes as the lateral pressure $P_\parallel$ becomes too small. For large confinement widths, $L_z > 3.25d$, the quadratic crystalline equilibrium state becomes unstable and the system favors a hexagonal crystalline configuration [1]. The corresponding shear-induced dynamics is expected to be significantly different since, for example, no depinning occurs. A closer investigation is beyond the scope of this study.

APPENDIX C: HYSTERESIS

The shear-induced laned and melted states are accompanied by strong structural transformations of the colloidal layers. They are related to very long relaxation times, and as a consequence one would expect hysteretic behavior of the shear stress as a function of shear rate. This is indeed the case, as shown in Fig. 16. Here, we have calculated the shear stress for two kinds of runs. For the first run, we started from the equilibrium configuration and successively increased the shear rate from $\dot\gamma\tau = 0$ by small steps of $\Delta\dot\gamma\tau = 0.01$ to $\dot\gamma\tau = 100$. In each step we started from the final configuration from the previous step. In the second run, we did the opposite, starting with the hexagonal steady state for $\dot\gamma\tau = 100$, and we successively decreased the shear rate to zero. The data were averaged over ten independent runs of ten different systems. The results are compared to the steady-state results [see Fig. 10(b)], where the steady state was obtained by applying a constant shear rate to the equilibrium configuration, and the simulations were run until the steady state was reached.

For the increasing shear rate run, the transition to the laned, melted, and hexagonal states shifts to larger shear rates compared to the steady-state results. The range of the quadratic state is extended, which can be attributed to the fact that the noise-induced events initiating the breaking of the crystalline order are very rare close to the transition from the quadratic to the laned state. A similar argument can be applied for the extension of the laned state. Also, the range of the melted state is drastically increased. In fact, the system was not able to rebuild a fully crystalline hexagonal state during the whole run. We suspect that this behavior is due to defects, which were formed in the melted state and sustained thermal fluctuations for extremely long times.

For the decreasing shear rate run, the range of the hexagonal state is slightly extended toward smaller shear rates compared to the steady-state results. The transitions to the laned and quadratic states are shifted only slightly relative to the steady-state results. Overall, the hysteretic behavior is most dominant for the transition from the melted to the hexagonal state, due to the strong plastic deformations accompanying the melted state. The hysteresis for the transition between the quadratic and laned state, as well as the laned and melted state, is rather weak. Furthermore, the laned state appears in both runs, suggesting that the appearance of this state is independent of the initial configuration.

[1] A. Fortini and M. Dijkstra, J. Phys.: Condens. Matter **18**, L371 (2006).
[2] E. C. Oguz, A. Reinmueller, H. J. Schoepe, T. Palberg, R. Messina, and H. Loewen, J. Phys.: Condens. Matter **24**, 464123 (2012).
[3] T. Curk, A. de Hoogh, F. J. Martinez-Veracoechea, E. Eiser, D. Frenkel, J. Dobnikar, and M. E. Leunissen, Phys. Rev. E **85**, 021502 (2012).
[4] M. R. Khadilkar and F. A. Escobedo, Soft Matter **12**, 1506 (2016).

[5] A. A. Aerov and M. Krüger, Phys. Rev. E **92**, 042301 (2015).
[6] I. Cohen, T. G. Mason, and D. A. Weitz, Phys. Rev. Lett. **93**, 046001 (2004).
[7] M. Mehrabadi, D. N. Ku, and C. K. Aidun, Phys. Rev. E **93**, 023109 (2016).
[8] F. E. Mackay, K. Pastor, M. Karttunen, and C. Denniston, Soft Matter **10**, 8724 (2014).
[9] J. S. Myung, S. Song, and K. H. Ahn, J. Non-Newtonian Fluid Mech. **199**, 29 (2013).
[10] D. Wilms, S. Deutschlaender, U. Siems, K. Franzrahe, P. Henseler, P. Keim, N. Schwierz, P. Virnau, K. Binder, G. Maret, and P. Nielaba, J. Phys.: Condens. Matter **24**, 464119 (2012).
[11] L. Isa, R. Besseling, A. N. Morozov, and W. C. K. Poon, Phys. Rev. Lett. **102**, 058302 (2009).
[12] D. Genovese and J. Sprakel, Soft Matter **7**, 3889 (2011).
[13] S. Martens, A. V. Straube, G. Schmid, L. Schimansky-Geier, and P. Haenggi, Eur. Phys. J.-Spec. Top. **223**, 3095 (2014).
[14] U. M. B. Marconi and S. Melchionna, Langmuir **28**, 13727 (2012).
[15] U. Zimmermann, F. Smallenburg, and H. Loewen, J. Phys.: Condens. Matter **28**, 244019 (2016).
[16] L. Apaza and M. Sandoval, Phys. Rev. E **93**, 062602 (2016).
[17] C. Kreuter, U. Siems, P. Nielaba, P. Leiderer, and A. Erbe, Eur. Phys. J.-Spec. Top. **222**, 2923 (2013).
[18] H. Wioland, E. Lushi, and R. E. Goldstein, New J. Phys. **18**, 075002 (2016).
[19] W. Fornari, L. Brandt, P. Chaudhuri, C. U. Lopez, D. Mitra, and F. Picano, Phys. Rev. Lett. **116**, 018301 (2016).
[20] K. Yeo and M. R. Maxey, Phys. Rev. E **81**, 051502 (2010).
[21] T. H. Besseling, M. Hermes, A. Fortini, M. Dijkstra, A. Imhof, and A. van Blaaderen, Soft Matter **8**, 6931 (2012).
[22] J. J. Cerdà, T. Sintes, C. Holm, C. M. Sorensen, and A. Chakrabarti, Phys. Rev. E **78**, 031403 (2008).
[23] B. Lander, U. Seifert, and T. Speck, J. Chem. Phys. **138**, 224907 (2013).
[24] R. Messina and H. Lowen, Phys. Rev. E **73**, 011405 (2006).
[25] S. Grandner and S. H. L. Klapp, J. Chem. Phys. **129**, 244703 (2008).
[26] S. H. L. Klapp, Y. Zeng, D. Qu, and R. von Klitzing, Phys. Rev. Lett. **100**, 118303 (2008).
[27] T. A. Vezirov and S. H. L. Klapp, Phys. Rev. E **88**, 052307 (2013).
[28] T. A. Vezirov, S. Gerloff, and S. H. L. Klapp, Soft Matter **11**, 406 (2015).
[29] S. Gerloff and S. H. L. Klapp, Phys. Rev. E **94**, 062605 (2016).
[30] G. Morfill, U. Konopka, M. Kretschmer, M. Rubin-Zuzic, H. Thomas, S. Zhdanov, and V. Tsytovich, New J. Phys. **8**, 7 (2006).
[31] K. R. Sütterlin, A. Wysocki, A. V. Ivlev, C. Räth, H. M. Thomas, M. Rubin-Zuzic, W. J. Goedheer, V. E. Fortov, A. M. Lipaev, V. I. Molotkov, O. F. Petrov, G. E. Morfill, and H. Löwen, Phys. Rev. Lett. **102**, 085003 (2009).
[32] M. Ciamarra, A. Coniglio, and M. Nicodemi, J. Phys.: Condens. Matter. **17**, S2549 (2005).
[33] D. Helbing and P. Molnar, Phys. Rev. E **51**, 4282 (1995).
[34] D. Helbing, L. Buzna, A. Johansson, and T. Werner, Transport. Sci. **39**, 1 (2005).
[35] I. Couzin and N. Franks, Proc. R. Soc. London Ser. B **270**, 139 (2003).
[36] B. Comiskey, J. Albert, H. Yoshizawa, and J. Jacobson, Nature (London) **394**, 253 (1998).
[37] G. Gelinck, H. Huitema, E. van Veenendaal, E. Cantatore, L. Schrijnemakers, J. van der Putten, T. Geuns, M. Beenhakkers, J. Giesbers, B. Huisman, E. Meijer, E. Benito, F. Touwslager, A. Marsman, B. Van Rens, and D. de Leeuw, Nat. Mater. **3**, 106 (2004).
[38] D. Ermak, J. Chem. Phys. **62**, 4189 (1975).
[39] J. Rottler and D. J. Srolovitz, Phys. Rev. Lett. **98**, 175503 (2007).
[40] S. H. L. Klapp, D. Qu, and R. v. Klitzing, J. Phys. Chem. B **111**, 1296 (2007).
[41] A. Reinmüller, T. Palberg, and H. J. Schöpe, Rev. Sci. Instrum. **84**, 063907 (2013).
[42] J. Delhommelle, J. Petravic, and D. Evans, J. Chem. Phys. **119**, 11005 (2003).
[43] J. Dzubiella, G. P. Hoffmann, and H. Löwen, Phys. Rev. E **65**, 021402 (2002).
[44] H. Orihara and Y. Takikawa, Phys Rev. E **84**, 061120 (2011).
[45] F. Frahsa, A. K. Bhattacharjee, J. Horbach, M. Fuchs, and T. Voigtmann, J. Chem. Phys. **138**, 12A513 (2013).
[46] A. A. Aerov and M. Krueger, J. Chem. Phys. **140**, 094701 (2014).
[47] B. D. Todd, D. J. Evans, and P. J. Daivis, Phys. Rev. E **52**, 1627 (1995).
[48] In our study, we have focused on the stress tensor averaged over the whole system, where the MOP yields the same results.